

# Adsorption of colloidal particles by Brownian dynamics simulation: Kinetics and surface structures

Jeffrey J. Gray<sup>a)</sup> and Roger T. Bonnecaze<sup>b)</sup>

*Department of Chemical Engineering, The University of Texas at Austin, Austin, Texas 78712-1062*

(Received 17 May 2000; accepted 28 August 2000)

Careful control of the microstructure of an adsorbed monolayer of colloidal particles is important for creating nanostructured devices through self-assembly processes. We present a computational model study for self-assembly of colloidal or nanoscale particulate systems. We develop a new technique for simulating colloidal adsorption processes, and we examine the kinetics and the structure formation on the surface. The technique allows the simulation of a nonhomogeneous suspension with an open boundary that is in equilibrium with a bulk suspension of known volume fraction, including the mean-field forces from the bulk solution and particle flux between the simulation box and the bulk. Short-time kinetics follow a power law similar to the case of diffusion-limited adsorption. Long-time kinetics fit a 2/3-power law form [P. Schaaf, A. Johner, and J. Talbot, *Phys. Rev. Lett.* **66**, 1603 (1991)] and kinetic coefficients are calculated. The zeta potential of the particles is the dominant parameter controlling the final surface coverage, but the zeta potential of the adsorbing surface is the dominant control for the ordering of the adsorbed system. Particles with larger Debye layers (lower salt concentrations) order more easily. Jamming limit coverages are compared to existing equivalent hard-disk models and an energetic model. Since the process is kinetically frustrated, particle exclusion effects play a major role in determining coverage as well as structure. © 2001 American Institute of Physics. [DOI: 10.1063/1.1319317]

## I. INTRODUCTION

Colloidal particle adsorption is important in processes such as the manufacture of film or the adsorption of proteins onto a biomaterial or a wound surface. There is also interest in carefully controlling depositional processes for the manufacture of new optical and electronic devices with controlled nanostructures.<sup>1</sup> As structures of technological interest get smaller, “top down” manufacturing processes such as lithography may be supplemented by “bottom up” self-assembly methods. The adsorption of colloidal-scale particles onto a surface in an adsorption process has been suggested for assembly of photonic devices<sup>2</sup> and has already been used to assemble prototype “nanowires.”<sup>3</sup> Novel redox catalysts have also been proposed that are assembled by adsorption of particles.<sup>4</sup> Control of superlattice formation is an important issue for these materials, and the rapid development of these nanoscale applications has spurred theoretical interest in this field. Here, we explore the fundamental aspects of the self-assembly process through simulation of the adsorption of electrostatically-repulsive colloidal particles. We systematically vary particle and wall zeta potential, Debye thickness, and bulk particle concentration to identify specific effects. Our overall goal is to determine the adsorption process kinetics, coverage, and the microstructure of the surface.

The adsorption of colloidal particles is an ideal process to use to examine nanoscale self-assembly processes. As a

model problem, it is simple yet contains several elements common to self-assembled nanoscale systems. Particles interact energetically with each other, wall parameters control the strength and penetration distance of the external forcing potential, and thermal energy must be carefully moderated to allow the system enough freedom to find an organized state but not too much so as to destroy it. By studying this model system, we can begin to formulate theories for the self-assembly of more complex nanoscale systems.

Adsorption processes have been modeled in a variety of ways. The simplest and oldest model is that of Langmuir which takes into account the finite amount of space available on a surface. The Langmuir isotherm displays a linear response to particle (or molecular) concentration in the regime of low coverage and saturation at high surface coverage. The Langmuir model requires only the relative rates of adsorption and desorption and the saturation coverage to predict equilibrium coverages.

More complex models have attempted to overcome the shortcomings of Langmuir’s simple model. New effects to include are the structure of the adsorbed phase, the structure of the bulk phase, and microscopic details of the adsorption process such as the effect of diffusion on the surface. Three main classes of models have arisen. In order of increasing complexity, computational cost, and information produced, these are random sequential adsorption models, density functional theories, and dynamic simulations.

Random sequential adsorption (RSA) models have recently been reviewed.<sup>5</sup> They involve sequential addition of disks onto a surface with no surface diffusion allowed. Important contributions of RSA-type models include the deri-

<sup>a)</sup>Electronic mail: jeff@che.utexas.edu

<sup>b)</sup>Author to whom correspondence should be addressed. Electronic mail: rtb@che.utexas.edu

vation of the jamming limit of 0.547 in irreversible, no-diffusion, hard disk systems and the asymptotic kinetic approach to the limit as the inverse square root of time.<sup>6</sup> Variations have incorporated electrostatic interactions,<sup>7,8</sup> bulk hydrodynamics,<sup>9</sup> three-dimensional funneling effects of adsorbed particles,<sup>10</sup> effects of substrate shape and bulk flow,<sup>11</sup> and particle tethering.<sup>12</sup> RSA models are limited because they consider the adsorption of one particle at a time, and usually no surface diffusion on the substrate surface. The bulk process is not considered, and kinetic data do not directly correlate to numerical values of time but rather to the number of attempted particle placements on the surface.

A second line of research has focused on the inhomogeneous liquid structure due to the presence of the wall using density functional theory and other integral theories.<sup>13,14</sup> Contributions from this line of work include observing the structuring of the bulk suspension into layers and calculating the range of the depletion region next to the wall. For walls charged opposite that of the particles, particles continue to adsorb until the wall has effectively inverted its charge.<sup>15</sup> Then the structure of the liquid, beyond a depletion layer whose thickness depends on the total surface adsorption, is identical to the structure that forms near any oppositely charged wall. Variations include the effect of bulk mixtures.<sup>16</sup> Integral equation models, however, are limited by the fact that they do not consider surface structuring and effects of size exclusion. They cannot give insight into the structure of the adsorbed phase. Finally, density functional theories have only been used to determine equilibrium states. Therefore, these studies have not contributed to process kinetics or determination of kinetically-frustrated states.

The last line of research is dynamic simulations, which can observe both equilibrium and nonequilibrium kinetically-frustrated states. Because dynamic simulations follow the motion of many particles explicitly in both the bulk and adsorbed phase, they offer the most information about the adsorption process but at the highest computational cost. Also, dynamic simulation is not trivial to perform. One notable complication is the boundary between the adsorbed and bulk phase. Homogeneous dynamic simulation techniques use periodic boundary conditions, but having an adsorbing boundary necessarily precludes this usual trick. One approach avoids the open boundary completely by treating two opposite edges of the box as adsorbing surfaces. This is an accurate simulation for a small slit, but not for a bulk system. First, the wall induces structure in the liquid, and a large simulation box is needed to capture the full structure. Second, adsorption of particles onto the surface rapidly depletes the volume fraction of particles in the bulk, causing a change in the chemical potential. It is difficult to perform a simulation and keep the bulk chemical potential constant.

Oberholzer *et al.*<sup>17</sup> developed one technique that overcomes this difficulty. Their Grand Canonical Brownian Dynamics scheme maintains the chemical potential by running a Monte Carlo simulation on the top portion of their simulation box at periodic intervals, thus replenishing the concentration in the box to make up for adsorbed particles. In essence, Oberholzer *et al.* have simulated adsorption from a well-mixed container where bulk diffusion and liquid struc-

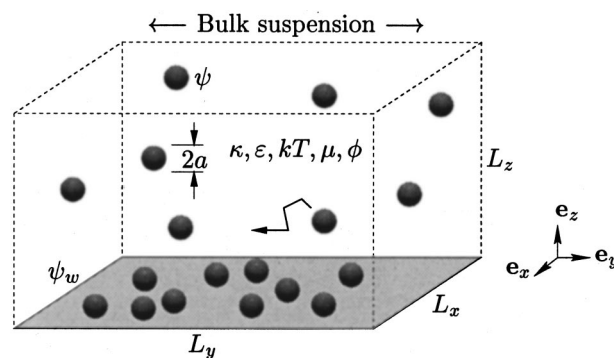


FIG. 1. Diagram of system.

turing do not play a major role. Oberholzer *et al.* applied their technique to study the effect of electrolyte concentration on kinetics and coverage of two specific adsorbents with fixed surface properties.

No studies to date have comprehensively examined the order-disorder transition of the surface structure or the dynamics of formation for an electrostatically-repulsive system. In addition, there is a need for systematic study of the effect of varying surface properties of adsorbent and adsorbate materials and suspension properties.

In this paper, we develop a new technique to maintain the correct chemical potential in the bulk yet still capture the complete dynamics of the adsorption process. We maintain an open boundary that is in contact with a bulk suspension of known volume fraction. This requires calculation of a mean-field force due to particles in the bulk acting on particles in the simulation box and algorithms to capture the flux of particles between the simulation box and the bulk. Our simulation scheme including these new techniques is detailed in Sec. II.

With this complete dynamic simulation, we systematically study colloidal adsorption for a range of particle potentials, wall potentials, volume fractions, and two Debye screening lengths. We compute kinetic parameters and identify the microstructure of the adsorbed phase. Finally, we emphasize adsorbed surface structures, important for the development of unique nanodevices. We identify order-disorder boundaries, examine models for surface coverage, and discuss the order-disorder transition. These results are presented in Sec. III, and discussion and comparison to models are presented in Sec. IV.

## II. FORMULATION

### A. Problem statement

Consider a semi-infinite suspension bounded by a wall (Fig. 1). The suspension contains a volume fraction  $\phi$  of spherical particles of radius  $a$ . The suspending fluid has viscosity  $\mu$ , an electrostatic permittivity  $\epsilon$ , and a Debye inverse screening length  $\kappa$  as determined by the ionic strength of the fluid. The density difference between the particles and the fluid is assumed to be negligible. Thermal energy in the system is characterized by  $kT$ , where  $k$  is Boltzmann's constant

and  $T$  is temperature. Particles are assumed to be Brownian, so we are considering particles with sizes ranging from 20 nm to 1  $\mu\text{m}$ .

Particles interact with each other and with the wall through colloidal double layer forces. Assuming pairwise interactions and low surface zeta-potentials, the forces are derived from the potentials

$$V_{iW} = 4\pi\epsilon a \psi \psi_w e^{-\kappa z}, \quad (1)$$

$$V_{ij} = 4\pi\epsilon a^2 \psi^2 e^{2\kappa a} \frac{e^{-\kappa r_{ij}}}{r_{ij}}, \quad (2)$$

where  $V_{iW}$  is the potential between particle  $i$  and the wall,  $V_{ij}$  is the potential between particles  $i$  and  $j$ ,  $\psi$  and  $\psi_w$  are the surface zeta-potentials of the particles and the wall, and  $r_{ij}$  is the distance between the centers of particles  $i$  and  $j$ . The forces are then

$$\mathbf{F}_{iW} = 4\pi\epsilon a \psi \psi_w \kappa e^{-\kappa z} \mathbf{e}_z, \quad (3)$$

$$\mathbf{F}_{ij} = 4\pi\epsilon a^2 \psi^2 e^{2\kappa a} \left( \frac{1}{r_{ij}} + \kappa \right) \frac{1}{r_{ij}} e^{-\kappa r_{ij}} \mathbf{e}_{r_{ij}}, \quad (4)$$

where  $\mathbf{F}_{iW}$  is the force between particle  $i$  and the wall,  $\mathbf{F}_{ij}$  is the force between particles  $i$  and  $j$ ,  $\mathbf{e}_z$  is the unit vector in the  $z$  direction (normal to the adsorbing surface), and  $\mathbf{e}_{r_{ij}}$  is the unit vector along the line of centers of the particles. Note that corrections to Eqs. (1)–(4) for finite ion size<sup>18</sup> can be easily included with changes only to the scaling parameters and not the functional forms.

The motion of each particle in the suspension is modeled with the Langevin equations,

$$\dot{\mathbf{x}}_i = \frac{\mathbf{D}_i}{kT} (\mathbf{F}_i^P + \mathbf{F}_i^B), \quad (5)$$

where  $\dot{\mathbf{x}}_i$  is the velocity vector of particle  $i$ ,  $\mathbf{D}_i$  is the diffusivity tensor of particle  $i$ , and  $\mathbf{F}_i^P$  represents the deterministic forces acting on particle  $i$  calculated assuming pairwise-additivity.  $\mathbf{F}_i^B$  represents the Brownian forces acting on particle  $i$ , with the hydrodynamic interactions between particles neglected in the diffusivity tensor. The Brownian force is characterized by the ensemble averages

$$\langle \mathbf{F}_i^B(t) \rangle = \mathbf{0} \quad \text{and} \quad \langle \mathbf{F}_i^B(0) \mathbf{F}_i^B(t) \rangle = 2\mathbf{D}_i^{-1} kT \delta(t), \quad (6)$$

where  $\delta(t)$  is the Dirac delta function.

The diffusivity  $\mathbf{D}_i$  is directly related to the mobility,

$$\mathbf{D}_i = kT \mathbf{M}_i. \quad (7)$$

Interparticle hydrodynamic interactions can reasonably be neglected because the volume fraction of particles is small. At  $\phi = 0.01$ , the average nearest-neighbor distance in the bulk is  $8.4a$ , and hydrodynamic coupling transmits less than 10% of transverse forces and less than 20% of normal forces to a nearest-neighbor particle [Eq. (6-2.10) in Ref. 19]. On the surface, where particle concentration is higher, nearest-neighbor distances can be half of that in the bulk, and hydrodynamic coupling between particles can transmit 20%–40% of forces. However, at the surface, lubrication interactions with the wall dominate the calculation of the mobility tensor.

Therefore, we approximate the mobility as a function of only the gap  $z$  between each particle and the wall,

$$\mathbf{M}(z) = \frac{1}{6\pi\mu a} [\tilde{M}_\perp(z) \mathbf{e}_z \mathbf{e}_z + \tilde{M}_\parallel(z) (\mathbf{e}_x \mathbf{e}_x + \mathbf{e}_y \mathbf{e}_y)], \quad (8)$$

where  $\tilde{M}_\perp(z)$  and  $\tilde{M}_\parallel(z)$  range from 0 to 1 and are the corrections to the mobility in the presence of the wall for motion perpendicular and parallel to the wall. Formulas for  $\tilde{M}_\perp(z)$  and  $\tilde{M}_\parallel(z)$  are tabulated in Appendix A.

## B. Scaling

The particle radius  $a$ , the thermal energy  $kT$ , the fluid viscosity  $\mu$ , and the electrostatic permittivity  $\epsilon$  are used to scale all the parameters in the problem to create nondimensional variables denoted with hats,

$$\hat{\mathbf{x}} = \frac{\mathbf{x}}{a}, \quad \hat{\kappa} = a\kappa, \quad \hat{t} = \frac{kTt}{6\pi a^3 \mu}, \quad \hat{\mathbf{x}} = \frac{6\pi a^2 \mu \dot{\mathbf{x}}}{kT},$$

$$\hat{\mathbf{F}} = \frac{a\mathbf{F}}{kT}, \quad \hat{V} = \frac{V}{kT},$$

$$\Psi = \left( \frac{4\pi\epsilon a}{kT} \right)^{1/2} \psi, \quad \Psi_w = \left( \frac{4\pi\epsilon a}{kT} \right)^{1/2} \psi_w,$$

and

$$\hat{\mathbf{D}} = \hat{\mathbf{M}} = \frac{6\pi\mu a \mathbf{D}}{kT} = 6\pi\mu a \mathbf{M}.$$

The nondimensional system is solved numerically, and in the remaining text, the nondimensional quantities are used and the hat notation is dropped for convenience.

## C. Numerical algorithm

The motion of a set of particles in a suspension is calculated within a box of dimensions  $L_x \times L_y \times (L_z + a)$ . The box is periodic in the  $x$  and  $y$  directions, and the wall is placed at  $z = -a$  so that the particle centers have a minimum coordinate of 0. The top of the box represents a boundary with the bulk fluid, and the height of the box is determined so that the volume fraction at the top boundary is not disturbed by the presence of the wall. Particles are initially placed at random positions within the box so that the volume fraction  $\phi$  matches that of the bulk. Each particle is tested to be sure that it does not overlap with other particles and that it is not within a distance closer than the bulk particle–particle depletion radius determined by a Monte Carlo simulation (Sec. II D). Particles are randomly repositioned if necessary.

Equation (5) has been discretized using a midpoint algorithm.<sup>20</sup> The motion of each particle is thus determined in a two-part time step,

$$\mathbf{x}_{i*} = \mathbf{x}_{it} + \frac{1}{2} \mathbf{D}(\mathbf{x}_{it}) \cdot [\mathbf{F}_i^P(\mathbf{x}_{it}) + \mathbf{F}_i^B(\mathbf{x}_{it})] \Delta t, \quad (9)$$

$$\mathbf{x}_{i,t+\Delta t} = \mathbf{x}_{it} + \mathbf{D}(\mathbf{x}_{i*}) \cdot [\mathbf{F}_i^P(\mathbf{x}_{i*}) + \mathbf{F}_i^B(\mathbf{x}_{i*})] \Delta t, \quad (10)$$

where  $\mathbf{x}_{it}$ ,  $\mathbf{x}_{i*}$ , and  $\mathbf{x}_{i,t+\Delta t}$  represents the positions of particle  $i$  at the beginning, midpoint and end of the time step, respectively. Re-evaluating the diffusivity and deterministic

forces at the midpoint increases the accuracy of the solution and correctly accounts for the variation of the diffusivity in space.

#### D. Mean-field forces from the bulk

In Eq. (5), the force acting on a particle  $\mathbf{F}_i^P$  is calculated by summing the particle-wall force and all pairwise particle-particle forces. The sum over all particles  $j \neq i$  in the simulation box is calculated in a straightforward manner, but interactions with particles in the bulk must be handled with a mean-field approximation, so that

$$\mathbf{F}_i^P = \mathbf{F}_{iW} + \sum_j \mathbf{F}_{ij} + \mathbf{F}_i^{\text{MF}}. \quad (11)$$

The repulsive force on particle  $i$  in the simulation box from particles in the suspension bulk is

$$\begin{aligned} \mathbf{F}_i^{\text{MF}}(\mathbf{x}) &= \int_{\Omega} n(\mathbf{y}) \mathbf{F}(\mathbf{y}-\mathbf{x}) d\mathbf{y} \\ &= \int_{\Omega} n g(r) \mathbf{F}(\mathbf{r}) d\mathbf{r} \\ &= \mathbf{e}_z \pi \int_H^{\infty} \left(1 - \frac{h^2}{r^2}\right) (n g(r) F(r)) r^2 dr, \end{aligned} \quad (12)$$

where  $\Omega$  is the volume of the bulk suspension above the simulation box,  $\mathbf{y}$  is a location in  $\Omega$ ,  $n(\mathbf{y})$  is the expected number density of particles at  $\mathbf{y}$ , and  $\mathbf{F}(\mathbf{y}-\mathbf{x})$  is the force created by a particle at  $\mathbf{y}$  onto particle  $i$  located at  $\mathbf{x}$  within the simulation box. In the second line,  $\mathbf{r}$  is the vector  $\mathbf{y}-\mathbf{x}$ ,  $r=|\mathbf{r}|$ ,  $g(r)$  is the equilibrium pair correlation function, and  $n=3\phi/4\pi$  is the number density of particles in the bulk. Inclusion of the pair correlation function  $g(r)$  in the calculation is necessary to accurately estimate the force in the case of large particle potentials where significant local structuring affects the particle arrangement. The pair correlation function is predetermined by a Metropolis method Monte Carlo simulation of the bulk suspension mixture.<sup>21</sup> Finally,  $h=L_z-z$  is the distance between the particle center and the top of the simulation box, and  $H$  is the maximum of 2 and  $h$ . In practice, the integral in Eq. (12) is pretabulated for rapid use during the simulation.

#### E. Grand canonical Brownian dynamics

The number of particles in the simulation box fluctuates in time. Occasionally a particle moves out of the top of the box and is lost into the bulk suspension. In the simulation this is handled in a straightforward fashion by simply eliminating particles with coordinate  $z > L_z$  at the end of a time step. According to the probabilistic rules of this Brownian system, particles from the bulk also wander into the simulation box. Handling the addition of particles is more complex.

The rate of flux of particles across a surface in a Brownian system can be shown (Appendix B) to be  $nA\sqrt{D/\pi\Delta t}$ , where  $n$  is the number density of particles,  $A$  is the area of the surface,  $D$  is the isotropic particle diffusivity in the bulk suspension, and  $\Delta t$  is the time interval over which the flux

occurs. The probability of observing a particle move into the simulation box from the bulk during a time step of duration  $\Delta t$  is then

$$P_{\text{flux}} = nL_xL_y\sqrt{\Delta t/\pi}. \quad (13)$$

Here we have used the fact that  $D=1$  in the bulk of the suspension due to the choice of scalings.

Particles that jump into the box appear at a range of depths from the top of the box. By calculating the distribution of jump sizes and initial particle locations (Appendix B), the location of a particle that wanders into the simulation box is

$$z = L_z - 2\sqrt{\Delta t}(-2 + \sqrt{4 - 2\ln q}), \quad (14)$$

where  $q$  is a random number uniformly distributed between 0 and 1. The  $x$  and  $y$  coordinates of new particles are chosen from a uniform random distribution over the area of the top of the box. Trial locations for new particles are tested and accepted with a Boltzmann factor,

$$\mathcal{P}_{\text{accept}} = \exp\left(\frac{V_{\text{new}} - V_{\text{bulk}}}{kT}\right), \quad (15)$$

similar to a Monte Carlo move.  $V_{\text{bulk}}$  is obtained from the Monte Carlo simulation of the bulk suspension.  $V_{\text{new}}$ , the potential of the new particle at the trial location, is calculated by summing the pairwise interactions with particles already present in the simulation box and the mean-field potential from particles in the bulk suspension (above the box). The mean-field potential is evaluated from

$$V_i^{\text{MF}}(h) = \int_{\Omega} n g(r) V(r) d\mathbf{r}, \quad (16)$$

where the variables and evaluation technique follows that in Sec. II D. If a new particle location is rejected according to Eq. (15), the new particle placement and acceptance procedure is repeated until a placement is accepted.

Simulations are performed on Unix workstations or a Cray T3E. Runs require 4 h to multiple days of CPU time.

### III. RESULTS

To our knowledge, the simulations presented here are the first to dynamically simulate adsorption using a box with an open top boundary. This method provides the most complete information about an adsorbing system: locations of adsorbed particles as well as particles diffusing through the bulk of the suspension. Evidence that the chemical potential in the bulk is correct in that the local volume fraction of particles at the open boundary is always equal to the selected simulation volume fraction. We set the vertical box size  $L_z$  to be large enough (usually  $40 \leq L_z \leq 100$ ) so that the depletion of particles due to adsorption never affects the concentration at the top of the box. Therefore, new particles are added to the box at an appropriate rate to simulate particles adsorbing onto a surface from a bulk suspension that is at rest. Horizontal box size and shape is set large enough to allow reasonable surface structures to form without major effects from the periodic boundary conditions. Usually,  $35 \leq L_x$ ,  $L_y \leq 80$  is sufficient. Near phase boundaries, multiple box sizes and



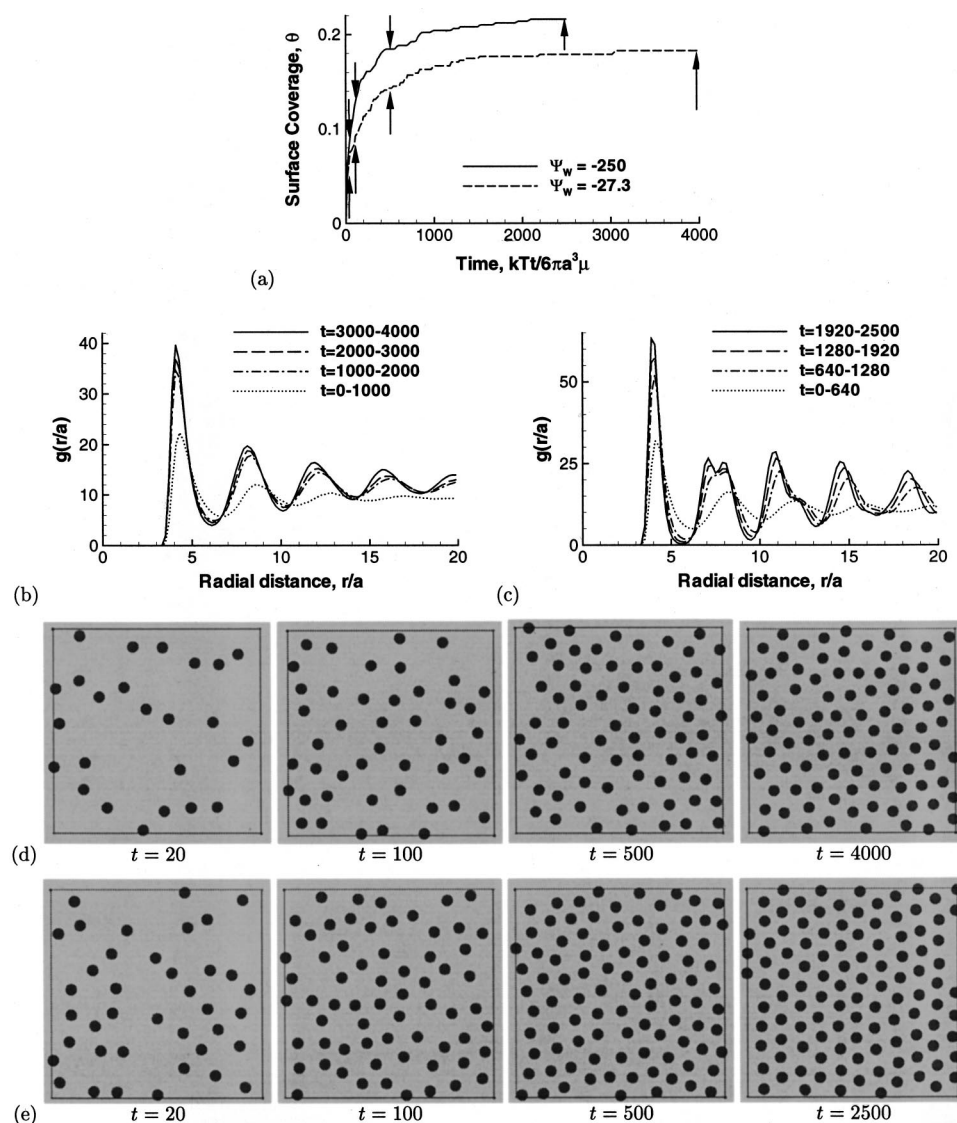


FIG. 2. Typical results from an adsorption simulation. (a) Adsorption kinetics for runs with two different wall potentials. In both simulations,  $\kappa=3$ ,  $\Psi=42$ , and  $\phi=0.01$ . Structure via the surface radial pair distribution function for (b)  $\Psi_w=-27.3$  and (c)  $\Psi_w=-250$  cases; Structure via direct observation for (d)  $\Psi_w=-27.3$  and (e)  $\Psi_w=-250$  cases. Arrows in (a) indicate the locations of the snapshots in (d) and (e). Probability distribution functions  $g(r/a)$  are normalized by the bulk suspension density and the monolayer thickness of one particle diameter to display the increase in surface structure and coverage over time.

rectangular shapes are tested to confirm structural results. Finally, the size of the time step varies from  $10^{-6}$  to 0.01. Repulsive interactions between particles stabilize the system and allow for larger timesteps, and smaller intervals are necessary only for low particle potentials or near phase boundaries.

Figure 2 shows typical results for two runs: one which forms an ordered adsorbed phase and one which does not, due to two different wall potentials. Figure 2(a) shows the kinetics of the process, Figs. 2(b)–2(c) show the structures as measured by the radial pair distribution functions on the surface, and Figs. 2(d)–2(e) show snapshots of the surface structures. For both runs, coverage increases rapidly at the beginning and slowly at the end when it reaches its steady-state value, with the steady-state coverage higher for the higher wall potential. The radial pair distribution functions are averaged over four equal time intervals over the course of the simulation and are normalized by the bulk suspension concentration. The development of the profiles over time reflects the accumulation of surface structure. The low wall potential case shows a medium-range liquidlike structure and the high wall potential case indicates order by the splitting

present in the second peak. These observations are confirmed by the snapshots of the adsorbed particles.

The kinetics of the processes can be examined more closely in their short-time and long-time limits, which are detailed in Secs. III A and III B, respectively. Surface coverages and structures of the adsorbed phases at the completion of the adsorption process are reported in Sec. III C. Finally, phase diagrams are presented in Sec. III D.

### A. Short-time kinetics

At short times, coverage increases roughly as the square root of time. Figure 3(a) shows kinetic data for one of the base case simulations of Fig. 2 with  $\Psi=42$ ,  $\Psi_w=-27.3$ , and  $\kappa=3$ . These short-time kinetic data are consistent with a diffusion-limited adsorption model, and indeed, the concentration profiles in the direction perpendicular to the adsorption surface [Fig. 3(b)] show an evolution consistent with a diffusion-limited system for times up to  $t=500$ , where the surface begins to saturate and the bulk structure begins to equilibrate. Near this point, the data in Fig. 3(a) diverge from the power law fit. Note that the power law fit to the short-time kinetic data actually has an exponent of 0.31 rather than

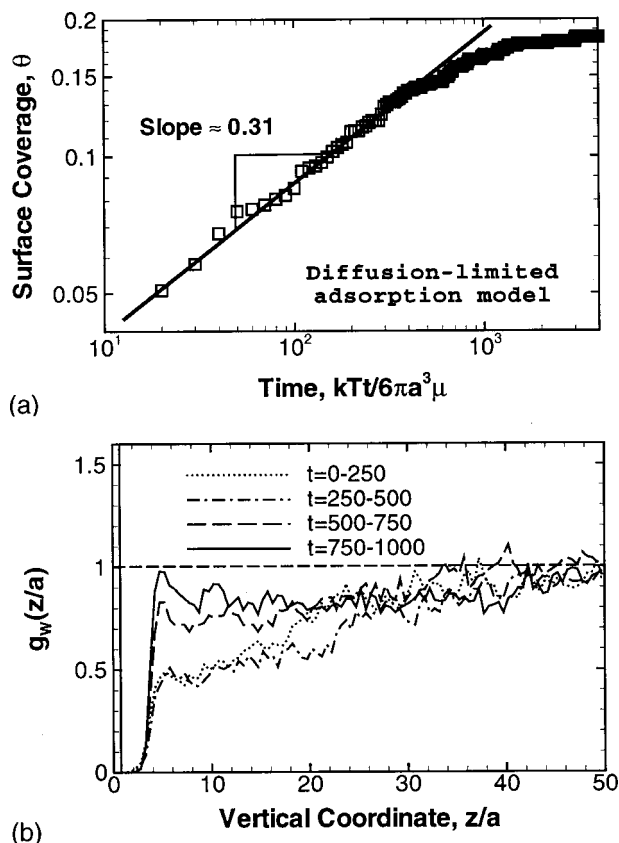


FIG. 3. (a) Logarithmic plot of the kinetic data from the  $\Psi_w = -27.3$  run in Fig. 2. The line represents a fit with slope 0.31. (b) Density profile in the vertical direction showing the penetration of particle depletion near the initial times of the adsorption process.

the theoretical 0.5. In fact, the nonidealities in the system cause the system to depart from a pure diffusion-limited system. In this section, we first summarize the case of diffusion-limited adsorption and how to compare to it, and then we present data for variations in particle volume fraction, particle- and wall-zeta potential, and electrostatic screening length.

The diffusion-limited adsorption (DLA) model is formulated by solving the nonsteady-state diffusion equation for an initially uniform, semi-infinite suspension with one boundary condition that acts as a perfect sink ( $\phi=0$  at  $z=0$ ) at finite times. Solving the unsteady-state diffusion equation,  $\partial\phi/\partial t = \partial^2\phi/\partial z^2$ , by a similarity transform and integrating the flux through the consuming boundary at  $z=0$  gives a total adsorption of

$$\theta(t) = \frac{3}{2\pi^{1/2}} \phi \sqrt{t}. \quad (17)$$

An example is shown in Fig. 4, which shows the short-time kinetics for runs with five volume fractions ranging from 0.0025 to 0.05 and the corresponding kinetics for the ideal DLA case. Note the deviation from the DLA model at higher volume fractions. To quantify the comparison of the simulation results with the DLA model, we fit a power law equation for each data set,

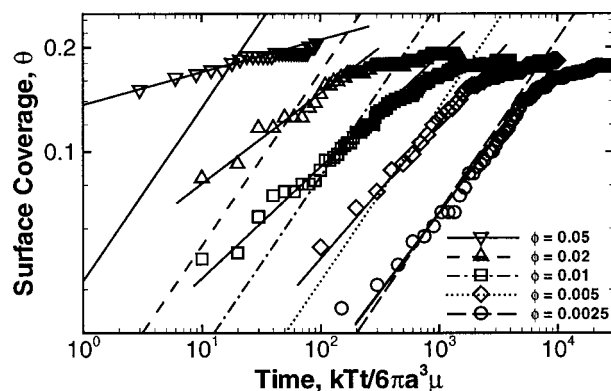


FIG. 4. Effect of volume fraction on short-time adsorption kinetics. Shown are simulation kinetic data (symbols), linear fits to the data (solid lines) and the ideal DLA model kinetics,  $\theta(t) = (3/2\pi^{1/2}) \phi \sqrt{t}$  (patterned lines). For all simulations,  $\kappa=3$  and  $\Psi_w = -27.3$ .

$$\theta(t) = A \frac{3}{2\pi^{1/2}} \phi t^B, \quad (18)$$

where  $A$  and  $B$  are parameters extracted from a linear fit on a logarithmic plot. The fitting constants  $A$  and  $B$  are shown in Figs. 5–7 for a range of run conditions. In general, the time exponent  $B$  ranges from the ideal value of  $1/2$  down to  $0.1$ . The coefficient  $A$  is always order 1.

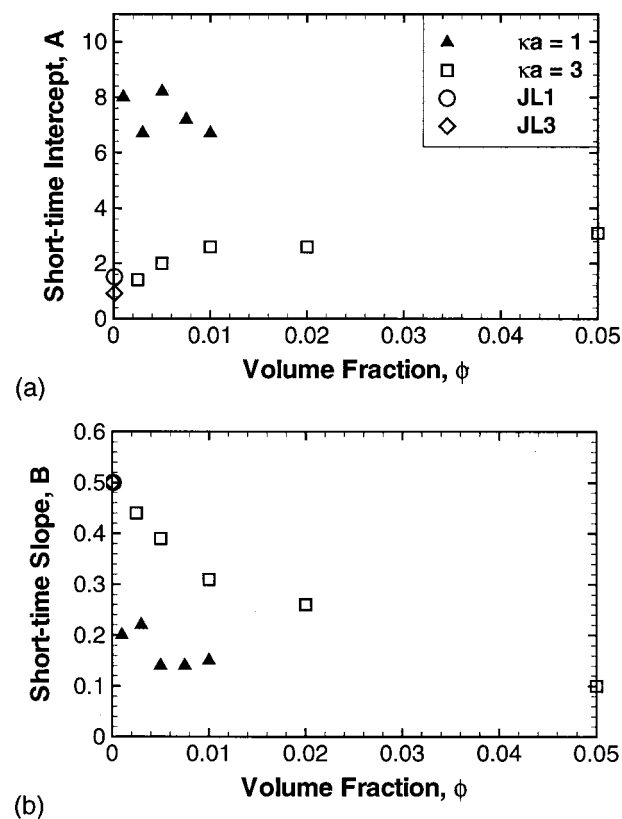


FIG. 5. Effect of volume fraction on short-time adsorption kinetics. Run parameters:  $\Psi=42$ ,  $\Psi_w = -27.3$ . In this and all subsequent plots, filled symbols represent runs that eventually reach ordered surface states, and open symbols represent runs that always remain disordered. “JL1” and “JL3” indicate data from Johnson and Lenhoff (Ref. 22) for  $\kappa=0.66$  and  $3 \leq \kappa \leq 27$ , respectively.

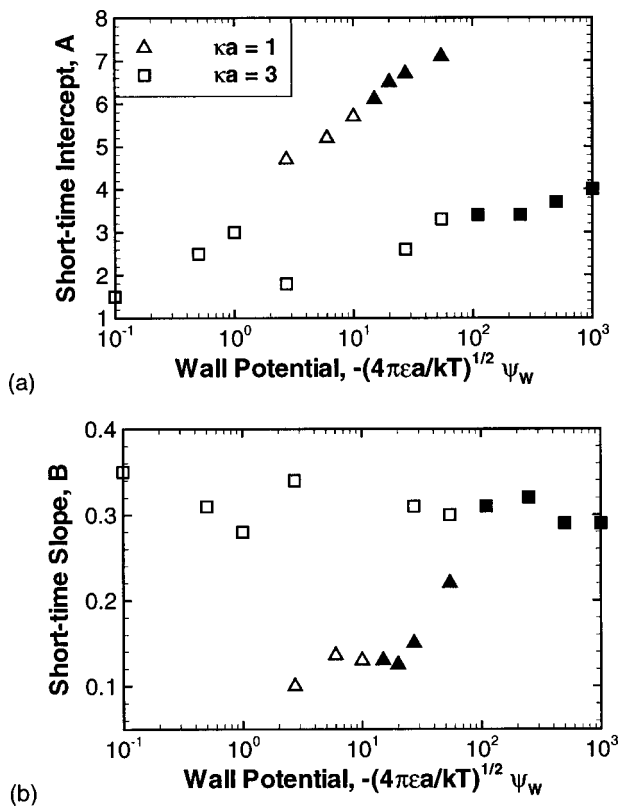


FIG. 6. Effect of wall potential on short-time adsorption kinetics. Run parameters:  $\Psi = 42$ ,  $\phi = 0.01$ .

The effect of volume fraction  $\phi$  on the short-time kinetic parameters is shown in Fig. 5 for Debye parameters  $\kappa$  of both 1 and 3. For  $\kappa = 3$ , the behavior is close to ideal ( $A = 1$ ,  $B = 1/2$ ) at low volume fractions, and as volume fraction is increased,  $B$  decreases and  $A$  increases. In contrast, the  $\kappa = 1$  runs are further from ideal and  $\phi$  has little effect on short-time kinetic parameters. Quantitatively, simulations with softer potentials ( $\kappa = 1$ ) adsorb much faster than those with harder potentials ( $\kappa = 3$ ).

The effect of the wall potential  $\Psi_W$  is shown in Fig. 6. For  $\kappa = 3$  the effect of  $\Psi_W$  is much more modest than the effect of volume fraction. However, in the  $\kappa = 1$  case, increasing  $-\Psi_W$  from 2 to 50 raises  $A$  from near 1 to 4 and  $B$  from 0.1 to 0.22.

The effect of particle potential  $\Psi$  is shown in Fig. 7 and is also drastic. Low particle potential cases are nearly ideal, with  $B$  near  $1/2$  and  $A$  near 1, and  $\kappa = 3$  runs are closer to ideal than  $\kappa = 1$  runs. As particle potential is increased for the  $\kappa = 3$  case,  $B$  decreases to 0.15 and  $A$  increases to near 5. Behavior is similar for the  $\kappa = 1$  case, although again, low  $\kappa$  runs proceed much faster. Note that several runs at lower  $\Psi$  have two data points reported. These data points correspond to two separate power-law kinetic regimes that are observed in some runs. An example is shown in Fig. 8.

Also shown in Fig. 7 are data from a set of runs examining the effect of changing the particle potential and wall potential in proportion, which is equivalent to controlling the temperature in a real system. For the most part, this temperature series follows the behavior of the particle potential series (both have  $\kappa = 3$ ), indicating that the wall potential plays

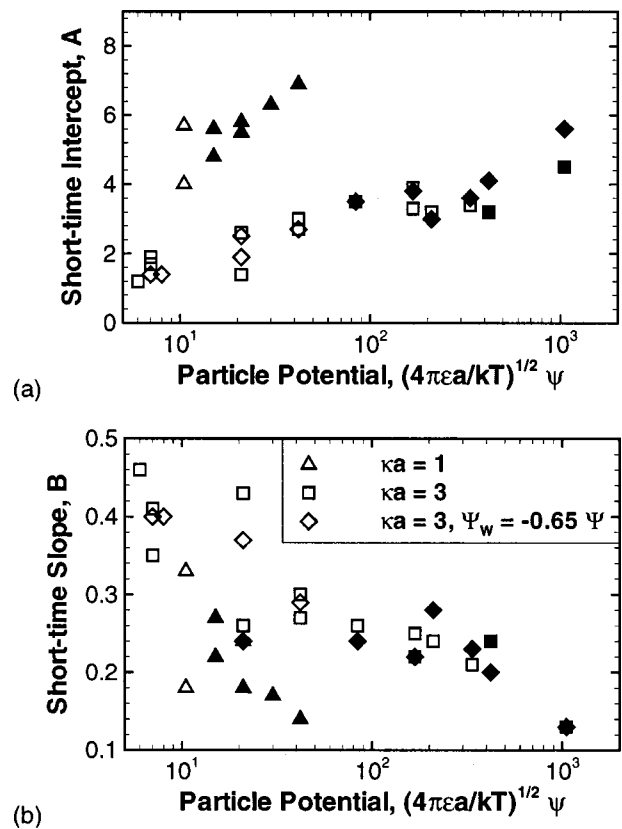


FIG. 7. Effect of particle potential on short-time adsorption kinetics. Run parameters:  $\phi = 0.01$ ,  $\Psi_W = -27.3$  except where noted.

a modest role at these simulation conditions. Finally, there is a small but noticeable jump in each data series near the order-disorder phase boundary of the system. These implications will be discussed later. Interpretation and discussion of all the short-time kinetic results follow in Sec. IV A.

## B. Long-time kinetics

At long times, coverage approaches a steady state. Figure 9(a) ( $\Psi = 42$ ,  $\Psi_W = -27.3$ ,  $\kappa = 3$ ) shows that, consistent with Schaaf *et al.*'s derivation for three-dimensional Brown-

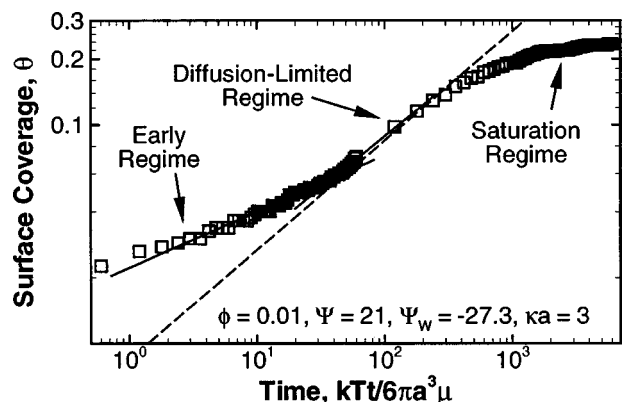
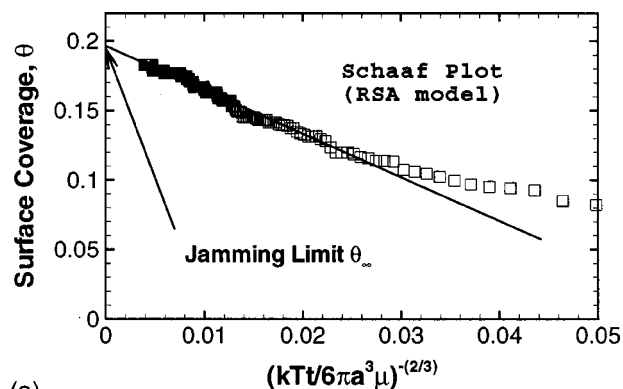
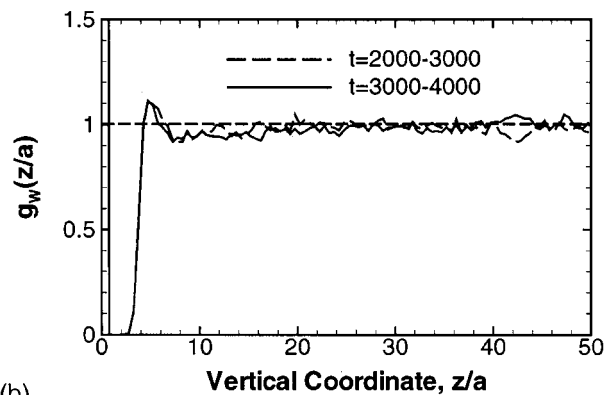


FIG. 8. Multiple kinetic regimes demonstrated for the case of  $\phi = 0.01$ ,  $\Psi = 21$ ,  $\Psi_W = -27.3$ ,  $\kappa = 3$ . Separate power law fits (solid lines) can be extracted for the early regime and the diffusion-limited regime. Also shown (dashed line) is the ideal DLA kinetic curve for a  $\phi = 0.01$  suspension.



(a)



(b)

FIG. 9. (a) Schaaf plot (Ref. 10) of the kinetic data from the  $\Psi_w = -27.3$  run in Fig. 2. The line represents a linear fit and extrapolates the data to an infinite time coverage  $\theta_\infty$ . The slope of the line yields the long-time kinetic coefficient  $\alpha$ . (b) Density profile in the vertical direction showing the pseudo-steady-state profile with a depletion region/energy barrier and liquid structuring.

ian adsorption,<sup>10</sup> the difference in jamming limit coverage and finite time coverage  $\theta_\infty - \theta(t)$  scales linearly with  $t^{-2/3}$ . The vertical density profile [Fig. 9(b)] clearly shows that the bulk structure is at steady-state. There is a depletion region near the wall, created by bulk-particle adsorbed-particle repulsions, and there is structuring in the liquid out to several particle diameters from the wall. Particles from the bulk periodically bombard the surface when they are able to overcome the energy barrier of the depletion region. These particles stick when they are able to find or create enough of a space in the surface adsorbed phase. This paradigm is equivalent to the assumptions in the RSA model, which is the model that Schaaf *et al.* used when deriving their asymptotic formula. The fit to Schaaf *et al.*'s asymptotic form is not surprising, except for the fact that the system that we model allows diffusion on the surface. Due to the strong attraction with the wall, the particle impact event probably occurs on a faster time scale than that of the surface-rearranging diffusion.

By fitting long-time kinetic data to Schaaf *et al.*'s form,<sup>10</sup>

$$\theta(t) = \theta_\infty - \alpha t^{-2/3}, \quad (19)$$

one can extract two fitted parameters: the jamming coverage  $\theta_\infty$  and the kinetic coefficient  $\alpha$ . The jamming coverages and the structures of the final adsorbed phases are presented in

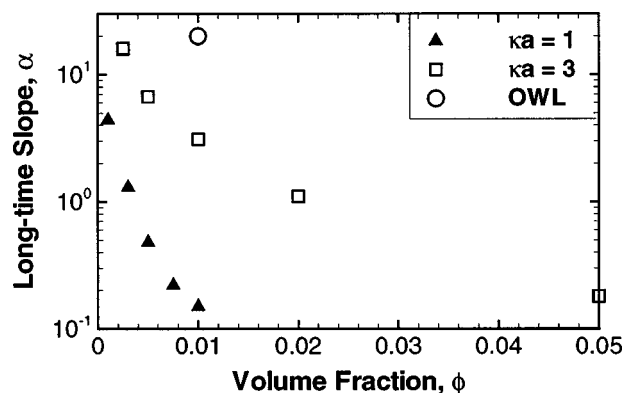


FIG. 10. Effect of volume fraction on long-time adsorption kinetics. Run parameters:  $\Psi = 42$ ,  $\Psi_w = -27.3$ . "OWL" indicates a datum from Oberholzer, Wagner, and Lenhoff (Ref. 17) at identical particle and wall potentials and  $\kappa = 3$ .

Sec. III C. Here, we describe the effect of the Debye parameter, volume fraction, and wall and particle potential on the long-time kinetic coefficient  $\alpha$ . Larger values of  $\alpha$  indicate faster approaches to the final steady-state coverage.

Figure 10 shows the effect of volume fraction on the long-time kinetic coefficient. For both Debye parameters  $\kappa = 1$  and  $\kappa = 3$ ,  $\alpha$  decreases almost two orders of magnitude as the volume fraction is increased, indicating a much slower approach to the jamming limit at higher volume fractions. Note that in the RSA derivation of Eq. (19), volume fraction is expected to scale equivalently as time ( $\theta \sim \phi^{-2/3}$ ) since impact frequency is proportional to both  $t$  and  $\phi$ . When the data are rescaled in this fashion (not shown), the drastic change in the kinetic coefficient is still not explained.

From the volume fraction series of data as well as those that follow, the Debye parameter  $\kappa$  can be seen to significantly affect the long-time adsorption kinetics.  $\alpha$  is always approximately one order of magnitude larger in the case of  $\kappa = 3$  compared to data from the case of  $\kappa = 1$ , showing the dramatic effect that salt concentration has on adsorption kinetics.

Wall potential has a mild effect on the long-time kinetics. In fact, for the case of  $\kappa = 3$ , the coefficient  $\alpha = 3.1$  for all runs, even though the final coverage values ranged from

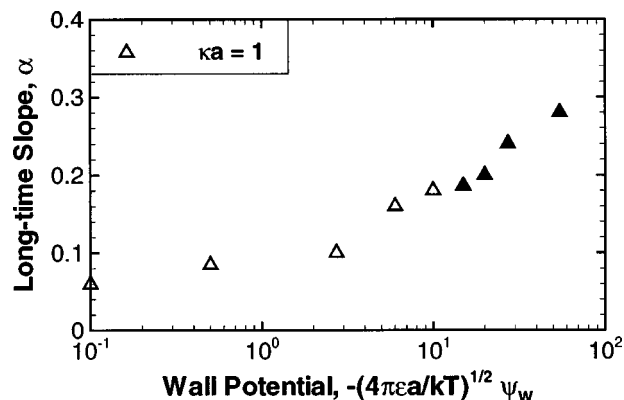


FIG. 11. Effect of wall potential on long-time adsorption kinetics. Run parameters:  $\kappa = 1$ ,  $\Psi = 42$ ,  $\phi = 0.01$ . For all  $\kappa = 3$  runs ( $\Psi_w$  ranges from 0.5 to 1000),  $\alpha = 3.1$ .



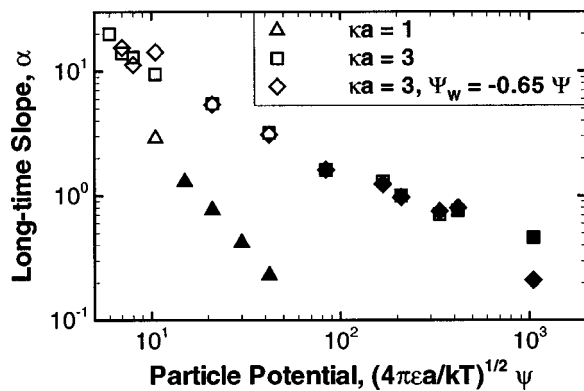


FIG. 12. Effect of particle potential on long-time adsorption kinetics. Run parameters:  $\phi = 0.01$ ,  $\Psi_w = -27.3$  except where noted.

0.16 to 0.29. For  $\kappa = 1$ ,  $\alpha$  increases from 0.052 to 0.30 as the wall potential magnitude increases from 0.1 to 54.6 (Fig. 11). Apparently, higher wall potential increases the rate of adsorption attempts even at high (long-time) surface coverages, but only for longer-ranged electrostatic interactions ( $\kappa = 1$ ).

The effect of particle potential is much more pronounced and is shown in Fig. 12. As particle potential is increased,  $\alpha$  decreases from 20 to 0.47 ( $\kappa = 3$ ) or from 4.13 to 0.23 ( $\kappa = 1$ ). A temperature series is also shown, and, like the short-time kinetic results, the temperature series shows behavior quite similar to the  $\kappa = 3$  particle potential series, indicating that the particle potential is much more dominant than the varying wall potential here.

### C. Coverage and structure at the jamming limit

Here, we report the jamming limit  $\theta_\infty$  results as determined from the extrapolation of the long-time fit in Eq. (19). In addition, we present the final structural results as various parameters are changed.

The Langmuir isotherm relates the adsorption coverage to the bulk concentration of a solute. Figure 13 shows the isotherm for the colloid system for two values of the Debye

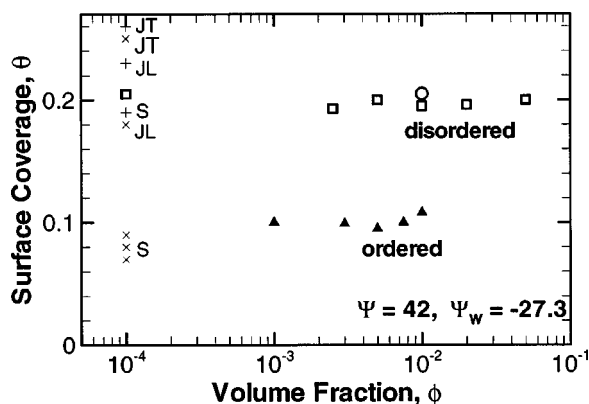
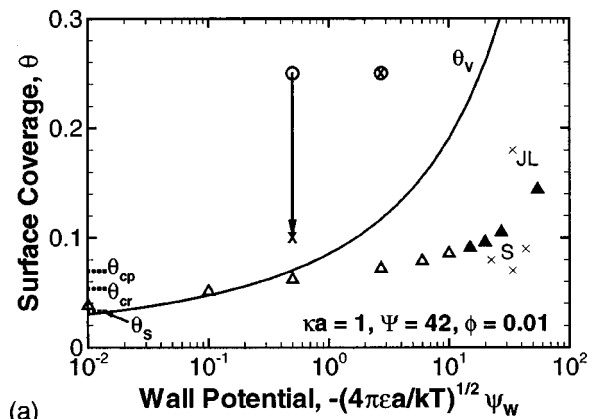
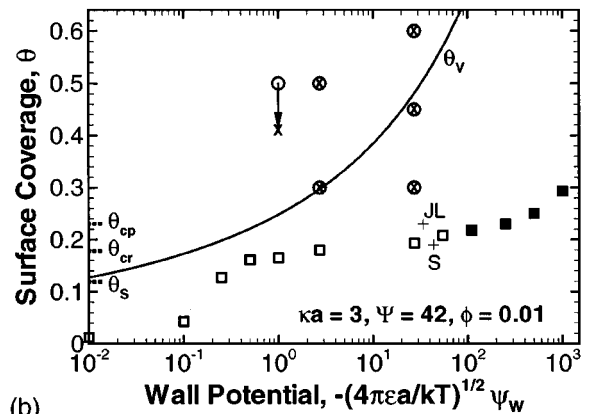


FIG. 13. Effect of suspension volume fraction on final surface coverage. Run parameters:  $\Psi = 42$ ,  $\Psi_w = -27.3$ ,  $\triangle$ ,  $\kappa = 1$ ;  $\square$ ,  $\kappa = 3$ ;  $\circ$ , denotes simulation result from Oberholzer *et al.* (Ref. 17). Experimental results shown as  $\times$  for  $\kappa = 1$  and  $+$  for  $\kappa = 3$  from Semmler *et al.* (Ref. 23) (S), Johnson and Lenhoff (Ref. 22) (JL), and Johnson (Ref. 24) (JT).



(a)



(b)

FIG. 14. Effect of wall potential  $\Psi_w$  on final surface coverage for (a)  $\kappa = 1$  and (b)  $\kappa = 3$ . Filled symbols represent runs that ordered during the course of the simulation, and open symbols represent runs that always exhibited disordered structures. Run parameters:  $\Psi = 42$ ,  $\phi = 0.01$ . Also shown are coverage predictions for various models:  $\theta_s$ , Semmler *et al.*'s coverage;  $\theta_{cr}$ , Russel *et al.*'s crystallization coverage;  $\theta_{cp}$ , Russel *et al.*'s close-packed coverage;  $\theta_v$ , energetic model coverage. Hexagonally-prepatterned surface runs are denoted with circles for initial surface coverages and  $\times$ 's for final surface coverages (also ordered structures). Experimental measurements are labeled as in Fig. 13.

screening parameter  $\kappa$ . For both screening lengths, the isotherm is flat, i.e., final adsorption coverage does not vary with bulk suspension volume fraction. This corresponds to the saturation regime of the Langmuir isotherm, and indicates that the adsorption in this system is practically irreversible. In fact, due to the strong interaction between the particles and the surface, no desorption of particles occurred during the finite time of these simulations. The effect of the Debye parameter is to lower coverage as  $\kappa$  is decreased. Lower  $\kappa$  corresponds to longer-ranged particle interactions and larger effective particle size, thus the lower coverage can be attributed to particle exclusion effects. The longer range of particle interactions also has a structural effect; all the  $\kappa = 1$  runs resulted in ordered surface structures, whereas the  $\kappa = 3$  runs resulted in random (disordered) surface structures. Also shown in Fig. 13 is a final coverage data point from the simulation study of Oberholzer *et al.*<sup>17</sup> Note that our results are in quantitative agreement.

Figure 14 shows the effect of wall potential  $\Psi_w$  on final surface coverage for two Debye parameters. For both curves, coverage is weakly dependent on wall potential, with cover-

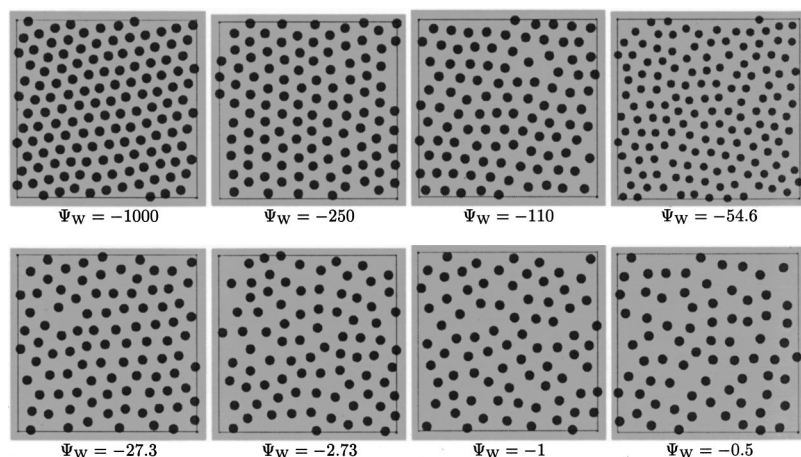


FIG. 15. Effect of wall potential  $\Psi_W$  on surface structures for  $\kappa=3$  runs shown in Fig. 14. Curves are displaced for clarity and normalized as in Figs. 2(b)–2(c).

age increasing with increasing magnitude wall potential. For very small wall potentials in the case of  $\kappa=3$ , the coverage falls off when the surface becomes effectively uncharged. For intermediate wall potentials for both  $\kappa$ , coverage increases modestly with wall potential, and for higher wall potentials the coverage increases more rapidly. The coverage is much higher for the case of  $\kappa=3$  than  $\kappa=1$ . Also, at high wall potentials, the surface structure changes from disordered to ordered, denoted in Fig. 14 by the change from open to closed symbols. Figure 15 shows several representative surface patterns as the system changes from disorder to order. Figure 16 shows the radial pair distribution functions for this set of runs. The ordered surface structures show distinct peaks due to the hexagonal surface pattern. The wall potential where peak-splitting disappears ( $\Psi_W = -110$ ) corresponds quite well to the point of loss of order by visual judgment. The peak-splitting criteria is used to formally distinguish between ordered and disordered phases in all runs.

Two-dimensional fluids of repulsive particles are known to have three equilibrium phases: a disordered liquid phase with short-ranged translational and orientational order, a hexatic phase with short-ranged translational order and quasilong ranged orientational order, and a crystal phase with quasilong ranged translational order and true long-range orientational order.<sup>25,26</sup> Unfortunately, computational speed

limits the size of our simulations to boxes too small to obtain adequate statistics for the precise determination of hexatic and crystal phases. The  $g(r)$  peak-splitting criterion that we employ is a surrogate for detailed analysis of the correlation functions over long ranges. The peak-splitting measure actually indicates the point where there is significant hexagonal order in the second shell of neighbors—this point corresponds well to the liquid-hexatic transition point.<sup>27</sup> Finally, the hexatic exists only over a small range of surface densities (1% in Ref. 26), thus most of the phases that we label “ordered” are likely to exhibit a crystal structure.

The effect of particle potential is shown in Fig. 17 for two values of the Debye parameter. Although increasing  $\Psi$  increases the coupling between the wall and the particles, increasing the particle potential causes jamming limit coverage  $\theta_\infty$  to decrease significantly due to increased particle–particle repulsions; from 0.29 to 0.11 for  $\kappa=1$  and from 0.43 to 0.086 for  $\kappa=3$  as the wall potential is varied. For both values of  $\kappa$ , the system orders at high particle potentials. In contrast to the ordering effect by changing the wall potential, here the ordering occurs as surface coverage is lowered. Two sample surface structures are shown in Fig. 18 and can be contrasted to those in Fig. 15.

As previously mentioned, varying temperature is equivalent, in scaled variables, to varying the particle and wall potentials simultaneously and holding  $\Psi/\Psi_W$  constant. Figure 17(b) shows the series of runs where  $\Psi_W$  is varied in proportion to  $\Psi$  coupled with the base series where only  $\Psi$  is varied. It is clear that the particle potential is the dominant parameter for controlling coverage, as the additional variation of the wall potential only changes the coverage slightly. However, the filled symbols in Fig. 17(b) show that at high wall potentials, several of the temperature-series systems create ordered phases at only slightly higher surface coverages than the corresponding runs of the constant wall potential series.

#### D. Phase diagram

Figure 19 shows the phase diagrams of ordered and disordered surface structures for a volume fraction of 0.01 and an inverse screening length  $\kappa=1$  and 3. The phase boundary is sloped, but it primarily runs along a line of constant wall

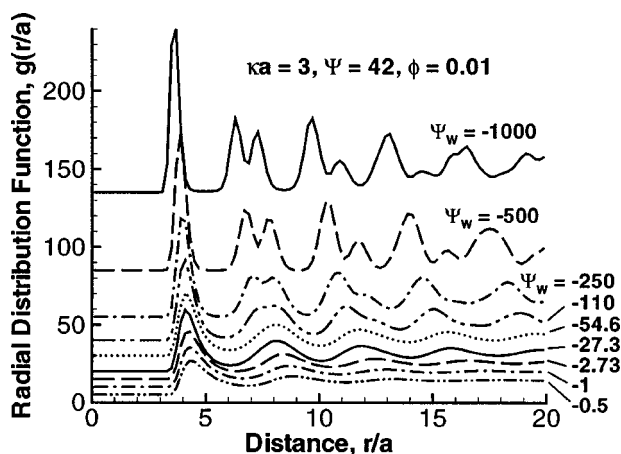


FIG. 16. Effect of wall potential  $\Psi_W$  on surface radial pair distribution functions for  $\kappa=3$  runs shown in Fig. 14.

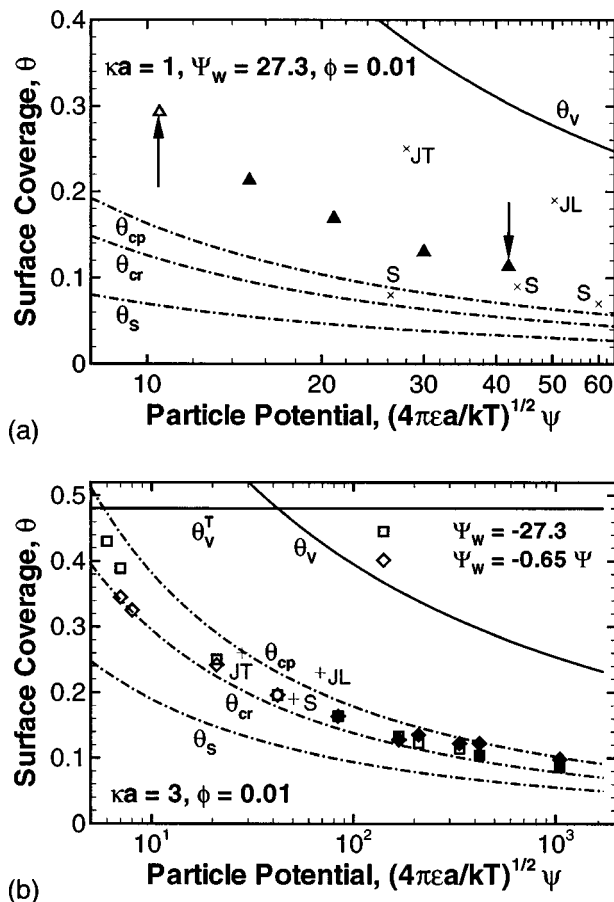


FIG. 17. Effect of particle potential on final surface coverage for (a)  $\kappa = 1$  and (b)  $\kappa = 3$ . Run parameters:  $\Psi_w = -27.3$ ,  $\phi = 0.01$ . Also in (b), effect of simultaneous variation of particle and wall potential (equivalent temperature). Also shown are coverages predicted by various models. (Symbols defined in Fig. 14 caption, except  $\theta_v^T$  which denotes the energy model coverage for the temperature series.)

potential. Clearly, the wall potential is the dominant factor in determining the microstructure of the adsorbed phase, and the particle potential has a weaker effect. The ordering boundary is at a lower magnitude wall potential ( $\Psi_w \approx -10$ ) for the case of  $\kappa = 1$  compared to the case of  $\kappa = 3$  ( $\Psi_w \approx -40$ ). Note that points in this figure are determined by examining the last simulation snapshot and the peak-splitting in the pair distribution over the last interval of time. There are two major sources of uncertainty in this determination; fortunately the errors may compensate each other. First, the finite box size used may stabilize the formation of an ordered phase. Second, the finite time may not be sufficient to allow crystallization to occur. To minimize these errors, long runs and runs with large boxes of varying aspect ratio were used for points near the phase boundaries, such that we expect the reported phase boundaries to be accurate.

#### IV. DISCUSSION

The simulations presented here are important for several reasons. They are the first to dynamically simulate adsorption of Brownian particles from a bulk medium at rest. The successful open boundary algorithms complete a tool that can be used to simulate other nonhomogeneous liquid sys-

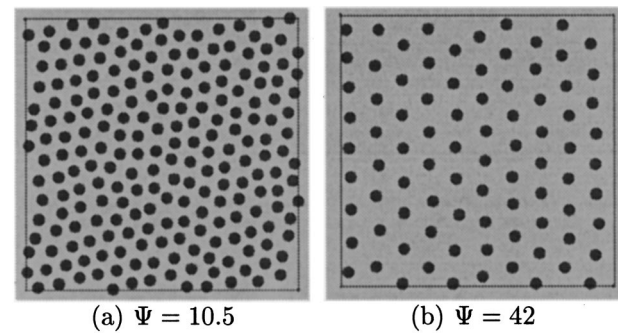


FIG. 18. Effect of particle potential on surface structure. (a) Disordered structure and (b) ordered structure corresponding to arrows in Fig. 17(a).

tems. Second, we have examined the kinetics of the adsorption process and extracted short- and long-time asymptotic behavior for energetically-interacting particles adsorbing to a long-ranged attractive boundary. Next, we have studied the final surface coverage and the phase behavior on the surface. In Sec. IV A we discuss the kinetic results and compare to experiments and other simulations. In Sec. IV B we examine surface coverage results, predictive models, and relevant experimental results. In Sec. IV C we discuss structure formation and how the simulation results can guide attempts to create micro- and nanoscale superlattice structures for novel materials and devices.

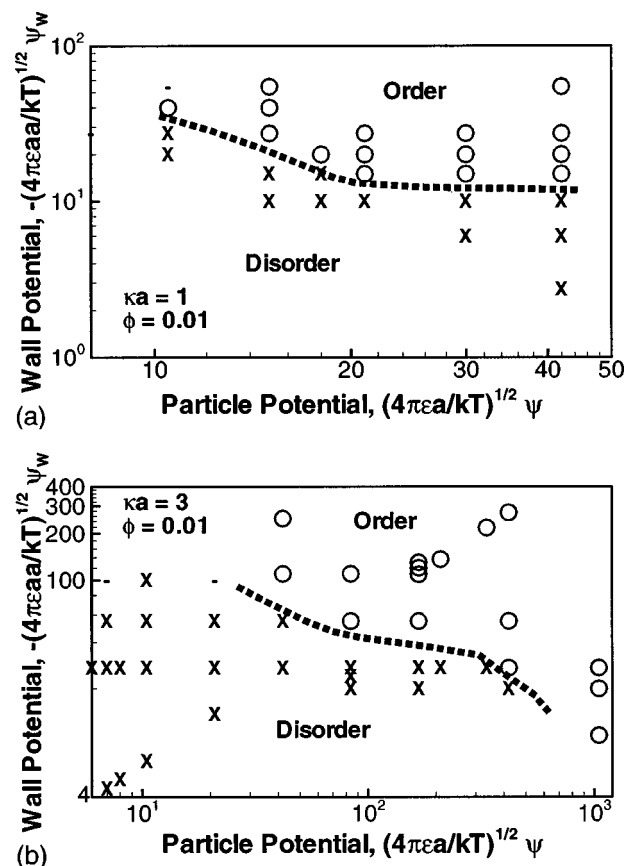


FIG. 19. Phase diagram of ordered and disordered adsorbed phases. (a)  $\kappa = 1$ ; (b)  $\kappa = 3$ . In both cases,  $\phi = 0.01$ . Dashes represent indeterminable runs due to numerical instabilities.



## A. Kinetics and applicable models

In Secs. III A and III B, we presented kinetic data for a range of particle volume fractions, wall potentials, particle potentials and two Debye lengths. The short time kinetic parameters ranged both near and far from an ideal diffusion-limited adsorption case, and here we would like to explore that deviation.

The conditions that create kinetics closest to ideal DLA include low volume fractions, low wall potentials, low particle potentials, and high Debye parameter. Under these conditions, the energetics of the wall attraction and the particle repulsions are minimized in magnitude as well as extent. As energetic interactions become important, the kinetic intercept  $A$  increases and the slope  $B$  decreases. The Debye parameter seems to have the strongest effect, with the most noticeable deviation from the ideal. Apparently, the range of the particle-wall and particle-particle interactions significantly affects the kinetics, as the  $\kappa=1$  simulations show much faster adsorption than  $\kappa=3$  simulations.

Most experimental measurements are taken at very low volume fractions.<sup>22–24</sup> Figure 5 includes data for  $\phi=10^{-4}$  extracted from experimental measurements of Johnson and Lenhoff.<sup>22</sup> Experimental short-time adsorption kinetics follow the DLA model closely, consistent with our findings for low volume fractions. Johnson and Lenhoff also see deviation toward faster adsorption for their lowest  $\kappa$  of 0.66, consistent with our findings where energetic interactions become important. Contrary to our trends, Semmler *et al.*<sup>23</sup> report a deviation from the DLA at their lowest volume fraction,  $\phi=10^{-5}$ . They attribute the deviation to the effects of some sort of convective currents, but it is unclear why convection would not occur also at their larger volume fractions. Due to the neglect of particle-particle hydrodynamic interactions and also limited system size, our simulations would not capture convective effects and we are unable to comment directly on this conjecture. However, the opposite trend of their experiments indicates either a possible measurement error on the extremely low volume fraction results in Semmler *et al.*'s work or a need for computationally challenging large-scale simulations including hydrodynamics.

At higher volume fractions, experimental data would be useful to validate our models. Higher volume fractions would be applicable to industrial processes for faster particle deposition using lower total volumes of feed suspension. It would be interesting to attempt to explore the kinetic deviation from the ideal using continuum models that include energetic interactions, perhaps similar in spirit to the existing density functional work.<sup>14</sup>

At long times, our kinetic data are consistent with the limited existing models. For all parameters, our data fit well to the 2/3-power law of Schaaf *et al.* for the adsorption of spheres. Some simulations that order exhibited some deviation from a linear fit, but this may have been related to finite box size effects upon the order-disorder transition. Power law kinetics apply well to ordered and disordered systems.

Variation in the long time kinetic coefficient  $\alpha$  arises, like the short-time kinetic parameters, due to variations in the thermal and energetic forces acting on the particle. Unlike the short-time kinetics, we have no "ideal" model with

which to compare our data. Certainly, as for short-times, higher volume fractions, larger particle potentials, and longer Debye lengths would be expected to increase the energetic contribution to the kinetics. From Figs. 10 to 12, one can see that these variations all lead to a decrease in  $\alpha$ , or slower kinetics. Johnson and Lenhoff's data follow a similar trend, at least for the variation in the Debye length shown in their Fig. 3. Finally, it is especially interesting that unlike the other energetic parameters, the wall potential has very little effect on long-time kinetics, even though the wall potential is the ultimate driving force for adsorption. This indicates that the rate limiting step is probably overcoming the energy barrier to adsorption created by the adsorbed particles.

There are currently no models that predict the long-time adsorption kinetic coefficient  $\alpha$ . Such a model might be able to explain the observed trends and illuminate the finer dynamics of this process.  $\alpha$  includes two contributions: the frequency of adsorption attempts and the success rate of adsorption attempts. The frequency depends on the dynamics of particles in the inhomogeneous distribution of particles near the surface. Particles from the first layer in the bulk must penetrate through the depletion layer [Fig. 9(b)] against the electrostatic repulsions of adsorbed particles. A model that could predict the frequency of adsorption attempts would be useful to relate RSA models to real time coordinates for electrostatically-interacting suspensions. Such a prediction might be possible by calculating fluctuation quantities from mean-field density functional theories.<sup>14</sup> The success rate of adsorption attempts would depend on particle position and interactions with particles on the surface, as well as the mobility of particles on the surface and the ability of the surface to accommodate an incoming particle. This calculation might be approximated with an appropriately modified RSA model.

It is appropriate here to point out some of the differences between our technique and that of Oberholzer *et al.*<sup>17</sup> While we have dynamically simulated the motion of particles inside a box that is tall enough to capture the effects of particle depletion in the bulk, Oberholzer *et al.*'s technique forcibly alters the distribution of particles in the suspension. Their grand canonical Brownian dynamics technique performs a Monte Carlo equilibration for the top portion of the box ( $z>L$ , where  $2.5\leq L\leq 5.75$ ) in regular intervals, replenishing any depletion of particles in the space above the adsorbing boundary. When our kinetic results are compared directly to those of Oberholzer *et al.*, our kinetics appear much slower. In fact, our results would be applicable for systems where adsorption occurs from a static bulk suspension. Oberholzer *et al.*'s technique mimics a system which has significant mixing of the bulk suspension at length scales very close to the surface.

At long times, both our technique and that of Oberholzer *et al.* would be expected to give similar results. Indeed, our final coverages agree, and like us, Oberholzer *et al.* found excellent agreement with Schaaf *et al.*'s kinetic form and used it to extrapolate to the jamming limit. Their kinetic coefficient, however, is several times higher than that found here (Fig. 10), reflecting again that the process they simulate is faster.



## B. Surface coverage and structure

To better understand the underlying causes behind the adsorbed surface coverage obtained in the simulations, we explore here simple existing models, and we develop an energetically based model. We then explore the nonequilibrium nature of the adsorption process and how that impacts the models appropriate for the system. We conclude with comparisons to experiment and connections between the kinetics and structure.

Simple models based on equivalent hard disk radii have previously been developed by Semmler *et al.*<sup>23</sup> adapting Russel, Saville, and Schowalter's<sup>28</sup> and Adamczyk and Warszyński's<sup>7</sup> methodology for examining the crystallization transition of electrostatically-stabilized colloidal suspensions. These models give rough estimates of surface coverages, but do not include the effect of surface structure or wall binding energy.

Russel *et al.*<sup>28</sup> describe a method of calculating effective hard sphere diameters for three-dimensional colloidal systems. Using this diameter, an estimate is made for the volume fractions for close packed configurations and the order-disorder transition. Russel *et al.* assign an effective hard sphere particle radius  $a_{\text{eff}}$  as the radial position where the electrostatic potential is a certain cut-off value. Inverting the potential equation [Eq. (2)], one obtains an infinite series expression that can be accurately approximated as

$$a_{\text{eff}} = (2\kappa)^{-1} \ln(A/\ln A), \quad (20)$$

with

$$A = \lambda \kappa \Psi^2 e^{2\kappa}, \quad (21)$$

where  $1/\lambda$  is the dimensionless cut-off potential. Adapting Russel *et al.*'s methodology to two dimensions and choosing  $\lambda = 1$ , the closest-packed surface coverage is calculated to be

$$\theta_{\text{cp}} = \frac{\pi}{2\sqrt{3}} (a/a_{\text{eff}})^2 = 0.9069(a/a_{\text{eff}})^2. \quad (22)$$

Russel *et al.* use the 3D hard sphere crystallization fraction to estimate the order-disorder transition. Modifying this for two-dimensional systems, we might expect the order-disorder transition to occur at

$$\theta_{\text{cr}} = 0.70(a/a_{\text{eff}})^2, \quad (23)$$

since systems of hard disks crystallize near the areal fraction 0.70.<sup>29</sup>

Semmler *et al.*<sup>23</sup> similarly predict jamming limits for random sequential adsorption model results. Semmler *et al.* found  $\lambda = 2.8$  to best fit experimental data, and they used the RSA jamming fraction of 0.547, predicting  $\theta_S = 0.547(a/a_{\text{eff}})^2$ .

In Fig. 17, Semmler *et al.*'s model and the modified Russel *et al.* models are plotted for particles with short-ranged ( $\kappa = 3$ ) and long-ranged ( $\kappa = 1$ ) interactions. Although all three models severely underpredict coverage in the  $\kappa = 1$  case, the  $\kappa = 3$  models can be constructively interpreted. Semmler *et al.*'s prediction represents the jamming limit of the RSA model, where diffusion is not allowed on the surface. Since our simulation allows surface diffusion,

the particles rearrange to allow denser coverage. Hence, Semmler *et al.*'s limit acts as a lower bound. The modified Russel *et al.* model assumes that the particles rearrange into a close-packed configuration, which is not always kinetically accessible or favored in this thermal system. The close-packed curve thus provides an upper bound to our data. The ordering boundary, however, is not consistent with our data at all. The model predicts ordered surface configurations for coverages above the line, and disordered configurations below the line. However, we see both ordered and disordered phases above the line, and the boundary seems to depend primarily on the wall potential. The wall potential is not included in any of the existing equivalent hard disk models, indicating a need for development of more general models.

A simple thermodynamic model can be constructed assuming that energetic forces dominate. Energetic contributions to the adsorbed phase can determine the cut-off potential which in turn determines the average particle-particle separation and surface coverage. This model can be derived differentially by considering the energetic contributions from the last particle to adsorb. The attractive energy between the new particle and the surface is balanced by the repulsive energy between adsorbed particles, which includes energy from the newly added particle and incremental repulsions between particles already adsorbed,

$$V_{pw} = \langle V_{pp} \rangle + N_{\text{ads}} \frac{\partial \langle V_{pp} \rangle}{\partial N_{\text{ads}}} = \langle V_{pp} \rangle + \theta \frac{\partial \langle V_{pp} \rangle}{\partial \theta}, \quad (24)$$

where  $V_{pw} = V_{iw}(z=0)$  is the binding energy of a particle on the surface,  $\langle V_{pp} \rangle = (z/2) V_{ij}(r_{ij} = \langle r \rangle)$  is the average particle-particle energy per particle,  $z$  is the coordination number of particles on the surface,  $\langle r \rangle$  is an average nearest-neighbor interparticle distance on the surface, and  $N_{\text{ads}} = \theta L_x L_y / \pi$  is the number of adsorbed particles. After separating  $\partial \langle V_{pp} \rangle / \partial \theta$  into  $(\partial \langle V_{pp} \rangle / \partial r)(\partial r / \partial \theta)$ , note that  $\partial \langle V_{pp} \rangle / \partial r = -\langle F_{pp} \rangle$  and  $\partial r / \partial \theta = -r/2\theta$  since  $\theta = 4\theta_{\text{max}} a^2 / r^2$ , where  $\theta_{\text{max}}$  is a maximum close-packed coverage. Substituting the particle-particle and particle-wall interaction potentials of Eqs. (1) and (2) yields the equation

$$\frac{1}{4} z \Psi e^{2\kappa} e^{-\kappa r} \left( \frac{3}{r} + \kappa \right) + \Psi_w = 0, \quad (25)$$

where  $r(\theta)$  here represents the average nearest-neighbor distance between particles on the surface. Assuming a hexagonal lattice ( $z = 6$  and  $\theta_{\text{max}} = \pi/2\sqrt{3}$ ), the coverage predicted by this model is indicated by the lines labeled  $\theta_V$  in Figs. 14 and 17.

The coverage predicted by the energy model is much higher than that observed in the simulations, indicating that the consideration of energetics alone is insufficient to describe the final coverage of adsorbed particles. In fact for  $\kappa = 3$ , the more simple hard disk model of Russel *et al.* is much better at predicting the coverage.

The energetic model does, however, turn out to be relevant to the equilibrium state of the adsorbed system. To test the state of the surface, we performed several simulations where the surface is prepatterned with hexagonal ordering and a high coverage of particles. If the jamming limit coverages were equilibrium coverages, one would expect the high-

coverage preloaded surfaces to undergo desorption until they reached the equilibrium coverages. However, if the final states were kinetically limited, the preloaded surfaces would maintain their high coverages. Initial and final coverages for these prepatterned runs are indicated in Fig. 14. For most prepatterned simulations, no particles left the surface. For simulations where particles did desorb, the surface quickly rearranged to maintain an ordered pattern. In order to observe desorption, it is necessary to preload the surfaces with coverages significantly higher than that predicted by the energetic  $\theta_V$  model, and the final coverages for these runs remain above the  $\theta_V$  prediction. Therefore, the coverages observed in these systems are kinetically limited, and particles continue to adsorb only as long as they can surmount the potential barrier presented by the layer of particles already adsorbed. Thus, the activation energy for adsorption increases with particle coverage. A particle from the bulk approaching a packed surface is much closer to the preadsorbed particles than to the actual surface. Especially in the case of short double-layers ( $\kappa=3$ ), a particle may not be able to feel the attraction of the wall. Even though the adsorbed state may be energetically favorable, it is very difficult for the particle to access this state. An equilibrium Monte Carlo simulation or integral equation model might, in fact, find the equilibrium for our  $\theta_V$  model, overpredicting the adsorption that is possible in a real system. Note that a RSA model including adsorption activation energies has been explored.<sup>8</sup>

It is difficult to map experimental conditions onto the dimensionless variables used in this study. We select points where  $\kappa=1$  or 3 and we estimate the zeta potential of particle and substrate surfaces from the available measurements in the experimental papers. Three sets of experiments are included in Figs. 13, 14, and 17. Similar to us, Semmler *et al.*<sup>23</sup> see coverage decrease rapidly for lower salt concentrations or longer Debye lengths. For  $\kappa\approx 3$ , they report coverages close to 0.2, similar to our base case results reported in Fig. 13. For  $\kappa\approx 1$ , they report lower coverages ranging from 0.07 to 0.09, compared to the 0.10 that we calculate. Johnson and Lenhoff's<sup>22</sup> and Johnson's<sup>24</sup> measurements are considerably higher, such that the  $\kappa=1$  results in particular are not consistent with ours. In Figs. 14 and 17, the data again seem consistent in magnitude, but not necessary in the trends observed. This is likely due to the difficulty of estimating  $\Psi$  and  $\Psi_w$  and controlling these parameters in experiment.

Structurally, experimental results differ from simulation results. Adsorption experiments have used particles that stick to the surface and can not rearrange to form ordered arrays as in this work.<sup>22–24</sup> These experiments produce only disordered surface structures. However, like us, for systems with longer Debye lengths, some report an increased degree of order as measured by the peak structures in the pair distribution functions.<sup>22,24</sup>

It is interesting to connect the discussion of the kinetics of the system with the discussion of the coverage and structure on the surface. Both kinetics and coverage are determined by the balance of particle–particle repulsions, wall attraction, and thermal energy or diffusion. It is possible, then, that one might be able to infer the controlling factors of

coverage by the controlling factors of the kinetics of a given system. Indeed, one can see in Fig. 7 that the trend of kinetic points undergoes a small jump near the order–disorder transition. Although the jump is small relative to the error in these measurements, it is notable and may be useful for predicting long-time structure given short-time kinetic information.

### C. Construction of colloidal and nanoscale structures

One of the primary goals of this study is to determine how colloidal and nanoscale structures can be assembled with particles. Varying the parameters of this simple model system reveals several guiding principles. First, the wall potential, which represents the background foundation upon which one assembles a structure, turns out to be very important in determining the final assembled structure. A large coupling between the surface and the particles forces the particles to form into ordered lattices. The particle energetics themselves play a much more minor role in determining final morphology. However, the particle–particle repulsions are the major determinant of interparticle distance and thus final coverage. In this system, it turns out to be simple to control coverage and structure almost independently using the particle and wall potentials. Finally, softer particle interaction potentials (low salt) favor the order in the system. Perhaps longer-ranged interactions stabilize long-range correlations. Also, short-range fluctuations are more easily tolerated with a long-range potential, favoring the global rearrangement into an ordered structure in favor of increased local entropy.

## V. CONCLUSIONS

We have successfully simulated the colloidal adsorption process using new techniques to model the open simulation boundary. Whereas RSA simulations are irreversible by design and usually allow no diffusion on the surface, we have performed complete dynamic simulations of adsorption from a bulk medium, and we have studied surface rearrangement into ordered and disordered microstructures. We have studied kinetics and quantified the departure from diffusion-limited adsorption due to energetic interactions between particles and the surface. Final surface coverage and structure are almost independently controlled by wall potential and particle potential, respectively, and we have presented phase diagrams delimiting the domains of ordered and disordered structures. Both the kinetic and the structural results reveal a need for predictive models, as these complex phenomena are not captured by any existing theories. We have begun to formulate general concepts on how colloidal and nanoscale particulate superassemblies can be designed and controlled, exploiting the simple model properties of our chosen system which includes a reservoir of pieces, a clean assembly surface, a forcing parameter in the wall potential, energetic interactions or couplings between particles, and thermal energy or entropic contributions.

## ACKNOWLEDGMENTS

We gratefully acknowledge the National Science Foundation (Grant No. CTS-9358409), the Packard Foundation

for a fellowship for R.T.B., the W. M. Keck Foundation and the University of Texas Thrust 2000 Program for a graduate fellowship for J.J.G., and the Texas Advanced Computing Center for computational resources.

## APPENDIX A: HYDRODYNAMIC MOBILITIES

The mobility components  $\tilde{M}_\perp$  and  $\tilde{M}_\parallel$  are determined assuming that particles interact hydrodynamically only with the wall. Close to the wall, the lubrication approximations hold<sup>30,31</sup>

$$\tilde{M}_\perp^{\text{lub}} = \left( 1.026\,375 + \frac{1}{\epsilon} - \frac{1}{21} \epsilon \ln \frac{1}{\epsilon} \right)^{-1}, \quad (\text{A1})$$

$$\tilde{M}_\parallel^{\text{lub}} = \left( 0.958\,8 + \frac{8}{15} \ln \frac{1}{\epsilon} + \frac{64}{375} \epsilon \ln \frac{1}{\epsilon} \right)^{-1}, \quad (\text{A2})$$

where  $\epsilon$  is the gap-width between the particle and the wall and is equal to the simulation coordinate  $z$ . The constant 1.026 375 has been chosen to match the outer solution. Far from the wall, far-field approximations apply<sup>19,30</sup>

$$\tilde{M}_\perp^{\text{ff}} = 1 - \frac{9}{8} h^{-1} + \frac{1}{2} h^{-3}, \quad (\text{A3})$$

$$\tilde{M}_\parallel^{\text{ff}} = 1 - \frac{9}{16} h^{-1} + \frac{1}{8} h^{-3}, \quad (\text{A4})$$

where  $h = z + 1$  is the distance between the wall and the particle center, scaled by the particle radius. For  $\tilde{M}_\perp$ , the lubrication solution is used for  $\epsilon < 1.328\,99$  and the far-field solution is used for  $\epsilon > 1.328\,99$ . For  $\tilde{M}_\parallel$ , the lubrication solution is used for  $\epsilon < 0.15$  and the far-field solution is used for  $\epsilon > 0.6$ . In the region  $0.15 < \epsilon < 0.6$ , a polynomial is fit to match the lubrication and far-field solutions,

$$\tilde{M}_\parallel^{\text{fit}} = 0.336\,72 + 1.299\,36\epsilon - 1.750\,05\epsilon^2 + 0.891\,86\epsilon^3. \quad (\text{A5})$$

In summary,

$$\tilde{M}_\perp = \begin{cases} \left( 1.026\,375 + \frac{1}{\epsilon} - \frac{1}{21} \epsilon \ln \frac{1}{\epsilon} \right)^{-1} & \epsilon < 1.328\,99, \\ 1 - \frac{9}{8} h^{-1} + \frac{1}{2} h^{-3} & \epsilon > 1.328\,99, \end{cases} \quad (\text{A6})$$

$$\tilde{M}_\parallel = \begin{cases} \left( 0.958\,8 + \frac{8}{15} \ln \frac{1}{\epsilon} + \frac{64}{375} \epsilon \ln \frac{1}{\epsilon} \right)^{-1} & \epsilon < 0.15, \\ 0.336\,72 + 1.299\,36\epsilon - 1.750\,05\epsilon^2 + 0.891\,86\epsilon^3 & 0.15 < \epsilon < 0.6, \\ 1 - \frac{9}{16} h^{-1} + \frac{1}{8} h^{-3} & \epsilon > 0.6, \end{cases} \quad (\text{A7})$$

where again  $h = \epsilon + 1$ .

## APPENDIX B: FLUX DERIVATIONS

The flux of Brownian particles through an arbitrary plane in the bulk of a suspension is calculated by integrating the probability for particles above a given plane to hop over the plane in an interval of time,

$$r_{\text{flux}} = \int_{\zeta=0}^{\infty} \frac{n \mathcal{P}(R > \zeta)}{\Delta t} d\zeta, \quad (\text{B1})$$

where  $r_{\text{flux}}$  is the number of particles to cross a unit area reference plane in a time interval  $\Delta t$ ,  $\zeta$  is a distance above the reference plane into the bulk suspension,  $n$  is the (uniform) particle number density, and  $\mathcal{P}(R > \zeta)$  is the probability of a particle making a hop of distance  $R$  that is greater than the distance  $\zeta$  and in the correct direction during the time interval.

According to the standard theory of Brownian motion, the probability that a particle will hop a distance  $\zeta$  is

$$\mathcal{P}(R = \zeta) = \frac{\exp(-\zeta^2/2\sigma^2)}{\sqrt{2\pi}\sigma^2} d\zeta, \quad (\text{B2})$$

where  $\sigma$  is the standard deviation of the particles' random jump, equal to  $\sqrt{2D\Delta t}$ . By integrating  $\mathcal{P}(R = \zeta)$  from  $\zeta$  to  $\infty$ , one finds

$$\mathcal{P}(R > \zeta) = \frac{1}{2} \operatorname{erfc}(\zeta/\sqrt{2}\sigma). \quad (\text{B3})$$

Substituting Eq. (B3) into Eq. (B1) and integrating yields

$$r_{\text{flux}} = \frac{n\sigma}{\sqrt{2\pi}\Delta t} = n \sqrt{\frac{D}{\pi\Delta t}}. \quad (\text{B4})$$

If  $A$  is the area of the top of the simulation box, the probability of a particle entering a box during a timestep of duration  $\Delta t$  is then

$$P_{\text{flux}} = r_{\text{flux}} A \Delta t = nA \sqrt{D\Delta t/\pi}. \quad (\text{B5})$$

Substituting  $D = 1$  for the scaled system produces Eq. (13).

Once a particle is known to have entered the box, the particle's initial depth into the box is calculated with a similar analysis. First one calculates the probability that a particle from the bulk will hop to a location at least a distance  $h$  below the plane of the top of the box. Using Eq. (B3) and the integral in Eq. (B1) with the lower integration limit  $\zeta = h$ , the number of particles that penetrates deeper than the depth  $h$  in a time interval  $\Delta t$  is

$$r_{\text{depth}}(h) = \int_{\zeta=h}^{\infty} \frac{n \operatorname{erfc}(\zeta/\sqrt{2}\sigma)}{2\Delta t} d\zeta. \quad (\text{B6})$$

Using some identities of the error function in the integration and converting the rate into a probability during a time interval [cf. Eq. (B5)], one obtains

$$P_{\text{depth}} = nA \sqrt{D\Delta t} \left[ \frac{1}{\sqrt{\pi}} \exp(-\tau^2) - \tau \operatorname{erfc} \tau \right], \quad (\text{B7})$$

where the substitution  $\tau = h/\sqrt{2}\sigma$  has been made for simplification. To determine penetration depth  $h$  from a random number generator, Eq. (B7) must be solved for  $\tau$  as a function of  $P_{\text{depth}}$ . Unfortunately, the equation does not yield an analytic solution. However, noting that the quantity in brackets is approximately  $\pi^{-1/2} \exp(-\tau^2/2 + 2\tau)$ , one can solve the equation algebraically, choose the physical root from the

resulting quadratic equation, and use Eq. (B5) to obtain

$$\tau \approx -2 + \sqrt{4 - 2 \ln \left( \frac{P_{\text{depth}}}{P_{\text{flux}}} \right)}. \quad (\text{B8})$$

Given that a flux event has been determined to occur,  $P_{\text{depth}}/P_{\text{flux}}$  is replaced by the random variable  $q$  uniformly distributed between 0 and 1, leading after substitutions to Eq. (14).

<sup>1</sup>S. H. Park and Y. Xia, *Langmuir* **15**, 266 (1999).

<sup>2</sup>J. D. Joannopoulos, P. R. Villeneuve, and S. Fan, *Nature (London)* **386**, 143 (1997).

<sup>3</sup>B. A. Korgel and D. Fitzmaurice, *Adv. Mater.* **10**, 661 (1998).

<sup>4</sup>S. D. Sitkiewitz, Ph.D. thesis, The University of Texas at Austin, 1999.

<sup>5</sup>J. Talbot, G. Tarjus, P. R. V. Tassel, and P. Viot, *Colloids Surf., A* **165**, 287 (2000).

<sup>6</sup>J. Feder, *J. Theor. Biol.* **87**, 237 (1980).

<sup>7</sup>Z. Adamczyk and P. Warszyński, *Adv. Colloid Interface Sci.* **63**, 41 (1996).

<sup>8</sup>M. R. Oberholzer *et al.*, *J. Colloid Interface Sci.* **194**, 138 (1997).

<sup>9</sup>I. Pagonabarraga *et al.*, *J. Chem. Phys.* **105**, 7815 (1996).

<sup>10</sup>P. Schaaf, A. Johner, and J. Talbot, *Phys. Rev. Lett.* **66**, 1603 (1991).

<sup>11</sup>Z. Adamczyk, B. Siwek, M. Zembala, and P. Belouschek, *Adv. Colloid Interface Sci.* **48**, 151 (1994).

<sup>12</sup>J. J. Gray, D. H. Klein, R. T. Bonnecaze, and B. A. Korgel, *Phys. Rev. Lett.* (submitted).

<sup>13</sup>N. Choudhury and S. K. Ghosh, *J. Chem. Phys.* **108**, 7493 (1998).

<sup>14</sup>P. González-Mozuelos and M. Medina-Noyola, *J. Chem. Phys.* **93**, 2109 (1990).

<sup>15</sup>P. González-Mozuelos and M. Medina-Noyola, *J. Chem. Phys.* **94**, 1480 (1991).

<sup>16</sup>P. González-Mozuelos *et al.*, *J. Chem. Phys.* **95**, 2006 (1991).

<sup>17</sup>M. R. Oberholzer, N. J. Wagner, and A. M. Lenhoff, *J. Chem. Phys.* **107**, 9157 (1997).

<sup>18</sup>J. E. Sader, *J. Colloid Interface Sci.* **188**, 508 (1997).

<sup>19</sup>J. Happel and H. Brenner, *Low Reynolds Number Hydrodynamics, With Special Applications to Particulate Media*, Prentice-Hall International Series in the Physical and Chemical Engineering Sciences (Prentice-Hall, Englewood Cliffs, 1965).

<sup>20</sup>P. S. Grassia, E. J. Hinch, and L. C. Nitsche, *J. Fluid Mech.* **282**, 373 (1995).

<sup>21</sup>M. P. Allen and D. J. Tildesley, *Computer Simulation of Liquids* (Oxford University Press, Oxford, 1987).

<sup>22</sup>C. A. Johnson and A. M. Lenhoff, *J. Colloid Interface Sci.* **179**, 589 (1996).

<sup>23</sup>M. Semmler, E. K. Mann, J. Rička, and M. Borkovec, *Langmuir* **14**, 5127 (1998).

<sup>24</sup>C. A. Johnson, Ph.D. thesis, University of Delaware, 1997.

<sup>25</sup>K. Chen, T. Kaplan, and M. Mostoller, *Phys. Rev. Lett.* **74**, 4019 (1995).

<sup>26</sup>K. Bagchi and H. C. Andersen, *Phys. Rev. Lett.* **76**, 255 (1996).

<sup>27</sup>J. J. Gray, Ph.D. thesis, The University of Texas at Austin, 2000.

<sup>28</sup>W. B. Russel, D. A. Saville, and W. R. Schowalter, *Colloidal Dispersions, Cambridge Monographs on Mechanics and Applied Mathematics* (Cambridge University Press, Cambridge, UK, 1989).

<sup>29</sup>B. J. Alder and T. E. Wainwright, *Phys. Rev.* **127**, 359 (1962).

<sup>30</sup>S. Kim and S. J. Karrila, *Microhydrodynamics* (Butterworth-Heinemann, Boston, 1991).

<sup>31</sup>A. J. Goldman, R. G. Cox, and H. Brenner, *Chem. Eng. Sci.* **22**, 637 (1967).